

1  
2  
3  
4  
5  
6  
7  
8  
9  
10  
11  
12  
13  
14  
15 **Population Spatial Frequency Tuning in Human Early Visual Cortex**  
16

17 Sara Aghajari<sup>1,2</sup>, Louis N. Vinke<sup>2,3</sup>, and Sam Ling<sup>1,2</sup>  
18

19 <sup>1</sup>Department of Psychological and Brain Sciences, Boston University, Boston, MA 02215

20 <sup>2</sup>Center for Systems Neuroscience, Boston University, Boston, MA 02215

21 <sup>3</sup>Graduate Program for Neuroscience, Boston University, Boston, MA 02215

22  
23  
24  
25 **Corresponding author:**  
26 Sara Aghajari  
27 677 Beacon St., Boston, MA 02215  
28 aghajari@bu.edu - T: (+1) 617-252-9483  
29

30  
31 SA performed research, analyzed data, wrote the first draft of the manuscript and edited it.  
32 LV collected and analyzed data, and edited the manuscript.  
33 SL designed and performed research, and edited the manuscript.

34  
35  
36

37

38

39 **Abstract**

40

41 Neurons within early visual cortex are selective for basic image statistics, including spatial frequency.  
42 However, these neurons are thought to act as band-pass filters, with the window of spatial frequency  
43 sensitivity varying across the visual field and across visual areas. Although a handful of previous fMRI  
44 studies have examined human spatial frequency sensitivity using conventional designs and analysis  
45 methods, these measurements are time-consuming and fail to capture the precision of spatial  
46 frequency tuning (bandwidth). In this study, we introduce a model-driven approach to fMRI analyses  
47 that allows for fast and efficient estimation of population spatial frequency tuning (pSFT) for  
48 individual voxels. BOLD responses within early visual cortex were acquired while subjects viewed a  
49 series of full-field stimuli that swept through a large range of spatial frequency content. Each stimulus  
50 was generated by band-pass filtering white noise with a central frequency that changed periodically  
51 between a minimum of 0.5 cpd and a maximum of 12 cpd. To estimate the underlying frequency  
52 tuning of each voxel, we assumed a log-Gaussian pSFT and optimized the parameters of this function  
53 by comparing our model output against the measured BOLD time series. Consistent with previous  
54 studies, our results show that an increase in eccentricity within each visual area is accompanied by a  
55 drop in the peak spatial frequency of the pSFT. Moreover, we found that pSFT bandwidth depends  
56 upon eccentricity, and is correlated with the pSFT peak; populations with lower peaks possess  
57 broader bandwidths in logarithmic scale, whereas in linear scale this relationship is reversed.

58

59

60 **Keywords:** spatial frequency, fMRI, visual cortex

61    **New and Noteworthy**  
62  
63    Spatial frequency selectivity is a hallmark property of early visuocortical neurons, and mapping these  
64    sensitivities gives us crucial insight into the hierarchical organization of information within visual  
65    areas. Due to technical obstacles, we lack a comprehensive picture of the properties of this sensitivity  
66    in humans. Here, we introduce a new method, coined population spatial frequency tuning mapping,  
67    which circumvents the limitations of the conventional neuroimaging methods, yielding a fuller  
68    visuocortical map of spatial frequency sensitivity.

69  
70  
71  
72

73     **Introduction**

74

75     The initial stages of visual perception are constructed from a handful of building blocks residing

76     within early visual cortex, including spatial frequency (SF; Watanabe et al., 1968, Wilson et al., 1983).

77     Spatial frequency sensitivity plays a crucial role in determining the degree to which a neural

78     population can discern the spatial scale of information processed within a visual scene. For instance,

79     neural populations that prefer low spatial frequency content can detect coarse luminance variations,

80     but are blind to fine details. Recordings from visual cortices in non-human primates have typically

81     found band-pass selectivity, wherein a visuocortical neuron displays peak sensitivity for a particular

82     SF, which is narrowly tuned to a range of neighboring frequencies. The neuronal response to

83     frequencies lower or higher than the peaked preference, however, drops off rapidly (DeValois et al.,

84     1982, Campbell et al., 1969, Movshon et al., 1978b).

85

86     Spatial frequency preferences in animal V1 indicate coarse structural organization, wherein the

87     distribution of spatial frequencies changes continuously across primary visual cortex (Issa et al., 2000,

88     Everson et al., 1998). Although neurons with receptive fields corresponding to the same visual

89     eccentricity tend to exhibit a wide range of SF sensitivities, the overall distribution of SF tuning

90     preferences gradually shift toward lower SFs as a function of eccentricity (Xu et al., 2007, Yu et al.,

91     2010). In addition to this retinotopically-organized drop-off in spatial frequency with eccentricity,

92     systematic variations of the peak preference have been observed across the visuocortical hierarchy, as

93     well. The mean peak SF preference at a particular eccentricity is roughly one third of the SF

94     preference found in the preceding visual area along the visuocortical hierarchy (Foster et al., 1985,

95     Movshon et al., 1978b, Issa et al., 2000). Interestingly, the bandwidth of spatial frequency tuning

96 appears to change as well, with electrophysiological recordings in cat V1 revealing an inversely  
97 proportional relation between peak and bandwidth of spatial frequency tuning, wherein neurons  
98 with preferences for higher spatial frequencies tend to have narrower bandwidths (DeValois et al.,  
99 1982).

100

101 To investigate the retinotopic organization of spatial frequency tuning in humans, a handful of  
102 studies have used functional magnetic resonance imaging (fMRI). From a methodological point of  
103 view these studies can be categorized into two groups: phase-encoding and stimulus-blocked designs.  
104 The phase-encoding approach is advantageous because it allows the peak spatial frequency tuning to  
105 be efficiently estimated for every individual voxel. Results using this approach are consistent with  
106 animal studies, replicating the negative correlation between peak SF preference and eccentricity  
107 (Sasaki et al., 2001). Although methodologically efficient, this approach is incapable of estimating the  
108 entire shape of the tuning curve for every voxel. Alternatively, other studies have employed  
109 conventional stimulus-blocked designs to estimate the shape of the tuning curve. Based upon these  
110 results, neural populations have been shown to act as simple linear filters, ranging from band-pass  
111 filters within V1 up to low-pass filters in V5 (Singh et al., 2000, Henriksson et al., 2008). In addition,  
112 similar to previous animal studies, the peak of the estimated tuning for V2 is less than that of V1, and  
113 the same is true for V3 relative to V2. Although blocked design studies have estimated the overall  
114 tuning function for certain visual areas, the estimation of the tuning curve per voxel requires the use  
115 of a large set of stimuli in order to attain enough statistical power, which becomes much less feasible  
116 when considering time constraints.

117

118 In this study, we set out to circumvent the aforementioned methodological limitations by proposing  
119 an alternative, model-based fMRI analyses approach (Dumoulin & Wandell, 2008; Kay et al., 2013;  
120 Zhou et al, 2018), which allows for the fast and efficient estimation of population spatial frequency  
121 tuning (pSFT) functions, at a voxel-wise level. By employing this novel technique, we were able to  
122 demonstrate rich and reliable measurements of spatial frequency tuning, both within and across early  
123 visual areas, allowing us to better examine the organization of spatial frequency selectivity in  
124 humans.

125

## 126 **Methods**

127 **Participants.** Eight subjects (3 females, median age = 28) participated in the study. Participants had  
128 normal or corrected-to-normal vision, and gave written informed consent to participate. The study  
129 was approved by the Boston University Institutional Review Board.

130

131 **Stimuli and Procedures.** Across each scan, participants viewed a set of stimuli that varied in spatial  
132 frequency content, ranging from a low 0.5 cycles per degree (cpd), to a high 12 cpd. Specifically, each  
133 stimulus was generated by filtering uniformly distributed noise with a narrow band-pass  
134 filter. The central SF of the band-pass filter (filter fixed-width: 0.1 cpd) spanned between 0.5 and  
135 12 cpd, sampled at 40 logarithmically spaced frequencies (Figure 1A). For each central SF, 10  
136 different versions were generated, each from a different initial noise distribution. The stimuli had  
137 a Michelson contrast of 90%, and were presented as a large annulus around fixation (outer diameter:  
138 19.6°; inner diameter: 0.32°). A fixation point was displayed at the center of the display, throughout  
139 the experiment (diameter of 0.1°). To promote fixation, the fixation point's color changed pseudo-

140 randomly on average every 4.5 seconds, and participants reported via key press the detection of these  
141 changes. All visual stimuli were generated using MATLAB (R2013a) in conjunction with the  
142 Psychophysics Toolbox-3 (Brainard, 1997; Pelli, 1997; Kleiner et al., 2007). All stimuli were  
143 displayed using a linearized VPixx PROPixx projector (maximum luminance: 389 cd/m<sup>2</sup>).

144

145 During each run, participants maintained their gaze on a fixation point at the center of the display,  
146 detecting the color change of the fixation dot. Simultaneously, a set of stimuli with varying spatial  
147 frequency content was displayed in the periphery. The peripheral stimulus changed continuously  
148 with a temporal frequency of 10Hz; however, the spatial frequency was updated in-synch with the  
149 scan sequence repetition time (TR = 1000ms, 1 Hz) (Figure 1B). Each spatial frequency from our  
150 selected set was presented six times during a run, and the order of presenting the frequencies was  
151 determined in a pseudo-random manner. Presentation of the stimuli started and also ended with a 10-  
152 second blank fixation period. Each participant completed a total number of 14 runs.

153

154 **fMRI Acquisition & Analyses.** All MRI data was collected on a Siemens 3T Prisma scanner using a 64-  
155 channel head coil. Responses to the varying spatial frequencies were measured during one two-hour  
156 session, and population receptive fields (pRF) were mapped during a separate session. In both  
157 sessions, BOLD activity was measured with simultaneous multi-slice echoplanar T2\*-weighted  
158 imaging (Moeller et al., 2010, Xu et al., 2013) with a field of view oriented perpendicular to the  
159 calcarine sulcus (2mm<sup>3</sup>; TR =1000ms; TE=35.40ms; FA=64°; FOV= 136\*136\*72mm). At the beginning  
160 of the main experiment, a T1-weighted anatomical volume with the same positioning as the  
161 functional runs was acquired (MPRAGE; 2mm<sup>3</sup>; TR=2530msec; TE=1.35msec; FA=7 ° ;

162 FOV=136\*136\*72mm). We registered the functional-matched T1 volume to a high-resolution  
163 reference anatomical T1-weighted whole-brain volume (MPRAGE; 1mm<sup>3</sup>; TR=2200ms; TE=1.54ms;  
164 FA=7°; FOV=256\*256\*256mm) acquired during a separate session. For each subject, this allowed us to  
165 align all the functional runs with the high-resolution anatomical volume, using an automated robust  
166 image registration algorithm (Nestares and Heeger, 2000). The mrTools neuroimaging analysis  
167 package (<http://gru.stanford.edu/mrTools>) was used to perform registration and standard  
168 preprocessing steps including motion correction, linear detrending, and applying a temporal high-  
169 pass filter (0.01 Hz). Before concatenating all times series across runs for each subject in preparation  
170 for the modeling fitting procedure, the within-run percent signal change for each voxel was  
171 computed by dividing the BOLD signal during each run by the mean. Additional data analyses were  
172 then carried out using custom code written in MATLAB.

173 We used population receptive field mapping (pRF) to delineate regions of interest (ROIs) V1–V3. The  
174 maps were acquired using standard techniques and stimuli (Dumoulin & Wandell, 2008; Kay et al.,  
175 2013), and data analysis was performed using the analyzePRF MATLAB toolbox (Kay et al., 2013).  
176 Only voxels lying within the occipital region were included in the pRF analysis, which were  
177 identified using an occipital lobe label generated from an atlas based upon intrinsic functional  
178 connectivity (Yeo et al., 2011).

179 The investigation of the spatial frequency preference dependency upon the preferred visual field  
180 position required having the parameters of both the pSFT and pRF analyses in alignment for each  
181 voxel. We used Freesurfer's boundary-based registration (Greve & Fischl, 2009) to bring the pRF  
182 analysis results into the pSFT functional session space. Then, by taking advantage of the capacity of  
183 mrTools to register individual functional runs to each other, while maintaining voxel-to-voxel

184 correspondence across different runs, we were able to extract BOLD responses of functional runs and  
185 the estimated pRF parameters for the same voxels across all ROIs.

186 **Population Spatial Frequency Tuning Modeling and Estimation.** Our modeling approach assumed a  
187 linear relation between the neural response and the BOLD response (Boynton et al., 1996, Birn et al.,  
188 2001, Hansen et al. 2004), allowing the concatenated BOLD response time series to be predicted by  
189 convolving the estimated population responses to the spatial frequencies of the stimuli that were  
190 presented, with a hemodynamic impulse response function (HIRM). In this study, we estimated the  
191 population spatial frequency tuning (pSFT) using a Gaussian function, for which the precise shape  
192 parameters are unknown (Henriksson et al., 2008, Farivar et al., 2017). With this assumed underlying  
193 model, we were able to synthesize an estimated BOLD response time series given the set of spatial  
194 frequency-varying stimuli presented in our imaging experiment. Since we were interested in  
195 assessing the unknown parameters in our pSFT model (preference and bandwidth) for each voxel, the  
196 synthesized time series from our pSFT estimates were iteratively fit to the measured BOLD response  
197 time series using a grid search to find the Gaussian model parameters that best aligned our  
198 synthesized and measured BOLD responses. We estimated the most accurate pSFT per voxel, by  
199 assuming a hypothetical model for the pSFT, and forcing its unknown parameters toward values that  
200 would result in the best fit between the synthesized and actual responses, given the examined spatial  
201 frequencies (Figure 2).

202  
203 Specifically, we assumed that the neural response to many different spatial frequencies is best  
204 captured by a log Gaussian distribution (Equation 1), expressed as:

205

206  $R(f) = e^{-\frac{(\log(f) - \log(\mu))^2}{2\sigma^2}}$  (1),

207

208 with two unknown parameters:  $\mu$  represents the peak, and  $\sigma$  is the standard deviation (std) that  
209 determines the spatial frequency tuning bandwidth. To find the parameters that best characterize the  
210 spatial frequency preferences of a voxel, we treated the BOLD signal as the product of a linear system  
211 (Boynton et al., 1996, Friston et al., 1994, Cohen 1997). This assumption allowed us to synthesize the  
212 BOLD response to the time series of spatial frequencies, ( $f(t)$ ), that were presented to subjects. The  
213 synthesized BOLD response  $B(t)$  is expressed as,

214

215  $B(t) = B_0 + \beta \cdot R(f(t)) * h(t)$  (2),

216

217 which is the product of the convolution of the neural response to the spatial frequencies,  $R(f(t))$   
218 with the HIRF,  $h(t)$ . The other two parameters,  $B_0$ , the baseline value, and  $\beta$ , the scaling factor,  
219 represent the changes in the baseline and scaling coefficient for the BOLD signal, respectively.  
220 Following the convention in neuroimaging analysis, both of these parameters were estimated using a  
221 general linear model (GLM) (Dumoulin & Wandell, 2008). To model the HIRF, we used a simple  
222 Gamma function (Boynton et al. 1996):

223

224  $h(t) = \frac{(t/\tau)^{(n-1)} e^{-(t/\tau)}}{\tau(n-1)!}$  (3)

225

226 In the equation,  $t$  is again time,  $n$  is the phase delay fixed at a value of 3, and the time constant  $\tau$  was  
227 set to 1.08. Moreover, in synthesizing the BOLD response, the delay between the stimulus onset and

228 the fMRI response was fixed at 2.05 seconds (Boynton et al., 1996). This model of the HIRF was  
229 selected over the 2-gamma HIRF (Glover 1999) mainly due to its simplicity. Reanalysis of the data  
230 with a 2-gamma function did not result in any substantial improvements nor changes in the  
231 qualitative pattern of results.

232

233 The coefficient of determination,  $R^2$ , between the synthesized signal,  $B(t)$ , and the real measured  
234 BOLD was used as a goodness-of-fit index. The two pSFT parameters, peak and bandwidth, that  
235 produced the highest  $R^2$  value yielded the optimal set of pSFT parameters. To find the optimal  
236 parameters that maximized the  $R^2$  we used exhaustive search. A grid comprised of the combination  
237 of 400 points for  $\mu$ , and 400 points for  $\sigma$  was used to search the peak-std space for optimal parameters.  
238 The  $\mu$  values were logarithmically spaced between 0.009 and 6, and the  $\sigma$  values were equally-spaced  
239 between 0.1 and 1. To exclude the estimations that tended toward the limits, in the final analysis,  
240 only voxels with peaks between 0.01 and 5, and bandwidths between 0.2 and 0.9 were included.

241

242 **Voxel Selection.** Considering the size of the stimuli, only voxels with pRF centers falling within the  
243 eccentricity range of 0.16°–9.8° were included in the final analyses. Moreover, voxels with poor fits  
244 in either the pRF or pSFT analyses were excluded. An  $R^2$  of 10% was set as the lowest acceptable  
245 goodness of fit for the pRF analysis. To set a threshold for the pSFT analysis, we carried out a  
246 permutation test, wherein sampling without replacement was used to shuffle the order of presented  
247 frequencies, generating a null distribution. The 95<sup>th</sup> percentile of the  $R^2$  of these estimates, across each  
248 cortical region, was calculated per subject, and finally the average of this value across all the subjects  
249 was set as the threshold for selecting voxels within that cortical area.

250

251 **Results**

252 To evaluate population spatial frequency tuning (pSFT) profiles, we deployed a generative model-  
253 based analysis (Dumoulin & Wandell, 2008, Kay et al., 2008, Harvey et al., 2013; Zhou et al., 2018),  
254 which allowed us to fit BOLD time series data with assumed underlying tuning parameters (detailed  
255 in Methods). We modeled the pSFT function as log Gaussian, with two primary unknown  
256 parameters: 1) mean, the peak spatial frequency preference, and 2) the standard deviation, that affects  
257 the selectivity bandwidth. Gaussian models have previously been used in neuroimaging studies to  
258 characterize spatial frequency tuning (Henriksson et al., 2008, Farivar et al., 2017), and the log  
259 Gaussian function fitted our data better in comparison to a linear Gaussian (One-tailed t-test of the  
260 difference of the medians of the  $R^2$  values;  $p<0.05$  for V1-V2). The model-based analysis involved  
261 iteratively fitting the BOLD time series data by changing the parameters of an assumed underlying  
262 model, in order to predict the best input/output relationship between the spatial frequency presented  
263 at a given moment and neural response. For any given sequence of spatial frequencies presented to an  
264 observer in a scan, the modeled neural response is transformed into a simulated BOLD response  
265 through convolution with an assumed hemodynamic impulse response function. The parameters  
266 (peak and std) that maximized the  $R^2$  of this fit were taken to be the final estimates for the pSFT of  
267 that particular voxel. Note that while the assumption of linearity between neural and BOLD response  
268 fails in certain regimes, the linearity approximation holds across quite a large range of conditions  
269 (Boynton et al., 1996, Birn et al., 2001, Hansen et al., 2004).

270

271 After estimation of the parameters, we first set out to qualitatively assess the organization of the  
272 estimated pSFT peaks across the visual field (Figure 3), using voxel-based retinotopic preferences  
273 derived from independent pRF mapping, per participant. Doing so revealed systematic changes in the  
274 peak spatial frequency selectivity with eccentricity. Consistent with previous reports (Sasaki et al.,  
275 2001, Henriksson et al., 2008, Hess et al., 2009), voxels with retinotopic preferences closest to the  
276 foveal confluence were selective for higher spatial frequencies, and this peak preference dropped off  
277 as a function of eccentricity. To focus on the eccentricity-based effects, in subsequent analyses we  
278 collapsed our results across polar angles (Figure 4A). This decline in peak spatial frequency preference  
279 with eccentricity emerged across all participants, and across visual areas V1–V3 (Figure 4B).

280

281 To quantify the precise nature of the relationship between eccentricity and peak spatial frequency  
282 preference, we fit the binned data with three candidate models proposed by previous work: Linear,  
283 Hinged line, and a Multiplicative Inverse Function. The three models that were fit on the mean peaks  
284 within eccentricity bins, are expressed as,

285

$$286 \quad \mu = A \cdot eccen + B \quad (4) \quad \text{Linear}$$

$$287 \quad \mu = A/eccen + B \quad (5) \quad \text{Multiplicative Inverse (M-Inverse)}$$

$$288 \quad \mu = \begin{cases} B & eccen < A \\ B + (eccen - A) \cdot C & eccen \geq A \end{cases} \quad (6) \quad \text{Hinged Line (H-Line)}$$

289

290 where  $\mu$  is the peak,  $eccen$  is the eccentricity and A-C are the unknown parameters, estimated  
291 separately for each function.

292

293 While a linear relationship has some support by Hess et al. (2009) and D’Souza et al. (2016), a hinged  
294 line relationship has been proposed as a plausible model, as well. Indeed, the hinged line has been  
295 used for describing the relationship between eccentricity and RF size in the past (Freeman &  
296 Simoncelli 2011). Moreover, this relationship between receptive field size and spatial frequency  
297 preference has been recently proposed as the central assumption behind the proposed single-unit  
298 receptive field (suRF) procedure (Keliris et al., 2019). To test the assumption that pRF size and spatial  
299 frequency sensitivity are related, we included this as candidate for modeling the eccentricity-spatial  
300 frequency sensitivity relationship, as well. This assumption is based on findings in simple cell  
301 recordings (Enroth-Cugell & Freeman 1987, Cleland et al. 1979). However, it is worth noting that  
302 evidence suggests that complex cells may diverge from this rule (Movshon et al. 1978a), and the  
303 existence of such relationship has been debated (Welbourne et al. 2018). Considering that there is  
304 evidence in favor of both possibilities, and we have measurements of both spatial frequency and pRF  
305 eccentricities acquired directly during an imaging session, we were able to test the possibility of a  
306 hinged line relationship in humans.

307

308 Alternatively, a multiplicative inverse function has been used as an approximation of the cortical  
309 magnification factor that changes along with visual eccentricity (Harvey and Dumoulin, 2011). The  
310 relationship between visual field coordinates and the corresponding retinotopic location of the  
311 representation across the early visual cortex has been shown to be well described by a complex  
312 logarithm function (Schwartz, 1977), the derivative of which is approximated by multiplicative  
313 inverse function (Schira et al., 2007). Although it has been argued that the exact magnification is not  
314 polar-invariant, this relationship is claimed to be a valid first order approximation (Schira et al.,

315 2010). In order to determine which model provided the best and simplest description of our results,  
316 we compared the AIC<sub>c</sub> (Corrected Akaike's Information Criterion) values of each model fit, which is  
317 a corrected variant that better accounts for a lower sample size (Hurvich & Tsai, 1989). The AIC<sub>c</sub>  
318 values for each model were transformed into the  $\Delta\text{AIC}_c$  values, which is simply the differences in  
319 AIC<sub>c</sub> values between a candidate model, and the minimum AIC<sub>c</sub> across the three models (Burnham &  
320 Anderson, 2002). The closer a  $\Delta\text{AIC}_c$  is to zero, the better that model is believed to account for the  
321 data relative to the other candidate models. Figure 5 is the mean  $\Delta\text{AIC}_c$  value across subjects,  
322 indicating that across V1–V3, the lowest AIC<sub>c</sub> value supports a multiplicative inverse relationship,  
323 wherein peak spatial frequency preference is the reciprocal of eccentricity (For individual subjects'  
324 fits, refer to the Supplementary Materials which are deposited in the Figshare repository at  
325 <https://doi.org/10.6084/m9.figshare.11499801.v1>). On a log-log scale, this manifests as a linear  
326 relationship between peak and eccentricity, from which we could then derive a parsimonious  
327 quantification of the drop-off with eccentricity (slope), and the peak spatial frequency tuning at the  
328 innermost eccentricity (intercept). Turning first to the slope estimates, the means of the fitted lines  
329 across subjects for V1 to V3 were respectively -0.49 (SD=0.10), -0.37 (SD=0.14), and -0.44 (SD=0.22),  
330 with all slopes being significantly negative ( $p<0.001$  for all regions) (Figure 4C). Despite a decrease in  
331 the overall spatial frequency preference from V1 to V3, the *rate* of drop-off in preference was  
332 preserved across visual areas, with no significant differences in slope found between areas (one-way  
333 ANOVA,  $F_{2,21} = 1.05$ ,  $p=0.37$ ). However, the intercept parameter, which served as a proxy for the  
334 peak preference at the innermost eccentricity, varied significantly across areas (one-way  
335 ANOVA,  $F_{2,21} = 3.93$ ,  $p=0.04$ ) (Figure 4D). A post-hoc Tukey test indicated that the differences were  
336 primarily between V1 and extrastriate visual areas (significant between V1 and V3,  $p=0.045$ , close to

337 significant in V1 vs. V2,  $p=0.086$ ). We converted the intercept back to spatial frequency by taking the  
338 exponential of the intercept, as this indicates the maximal SF represented within each of our cortical  
339 ROIs, and found the highest value in V1 (1.99 cpd, SD=0.28), which drops down in V2 (1.60 cpd,  
340 SD=0.24), and V3 (1.55 cpd, SD=0.46).

341

342 Psychophysical and neurophysiological studies suggest that perceptual sensitivity is impacted not  
343 only by eccentricity, but by anisotropies in perceptual sensitivity across polar angle, as well (Cameron  
344 et al., 2001; Carrasco et al., 2002; Rijksdijk et al., 1980; Levine and McAnany, 2005; Karim and Kojima,  
345 2010). To examine whether our estimated pSFTs reveal non-uniformities across the visual field, we  
346 leveraged pRF mapping to split the visual field into sections (Silva et al., 2018), allowing us to simply  
347 test for differences in the pSFT parameters between sets of quadrants of the visual field. The  
348 quadrants were comprised of 90° wedges above, below, left and right of fixation. In addition, the  
349 eccentricity range was divided into 10 equally-spaced bins. Figure 6 shows the mean of the pSFT  
350 peaks lying within these eccentricity bins, for different sets of quadrants. In V1, the peak in  
351 horizontal meridian quadrants is higher than the vertical meridian quadrants. Moreover, lower and  
352 left fields were slightly higher in SF preference, compared to the upper and right fields, respectively.  
353 Similar to Silva et al., 2018, we found differences in the mean peak within each bin, between the two  
354 opposing quadrants for every subject, and then carried out a two-tailed, one-sample t-test on these  
355 differences combined across subjects. For each subject, only bins that had at least one voxel within  
356 each of the two quadrants were included in the analysis. Differences were significant in V1 between  
357 horizontal and vertical meridian quadrants (V1:  $t(74) = 5.06, p < 0.001$ ; V2:  $t(76) = -0.42, p = 0.67$ ; V3:  
358  $t(68) = -1.89, p = 0.06$ ), as well as upper vs. lower (V1:  $t(61) = -3.86, p < 0.001$ ; V2:  $t(63) = -2.32, p =$

359 0.02; V3:  $t(51) = 0.01$ ,  $p = 1.00$ ), and right vs. left (V1:  $t(77) = -3.67$ ,  $p < 0.001$ ; V2:  $t(73) = 0.48$ ,  $p =$   
360 0.63; V3:  $t(64) = 1.05$ ,  $p = 0.30$ ). Except for the difference between upper and lower quadrants in V2,  
361 which primarily emerged in the periphery (Figure 6), we did not find meaningful differences in V2  
362 and V3.

363

364 To investigate voxel-wise SF selectivity, we first used the estimated parameters to calculate the pSFT  
365 bandwidths in octaves. The bandwidth of spatial frequency selectivity has traditionally been indexed  
366 in octave units in neurophysiological studies, due to the assumed logarithmic representational scaling  
367 of spatial frequency coding within the visual system (e.g. De Valois et al., 1982; Movshon et al.,  
368 1978b, Foster et al., 1985). Using octaves as a measure of bandwidth adheres to this ratio-based  
369 representation of spatial frequency, while also allowing for a symmetric measure of frequency tuning  
370 width. Considering that an octave is a frequency ratio of 2:1, the full bandwidth at half-amplitude in  
371 octave units is defined as the log transform of the ratio of the SFs at half-amplitude of the pSFT  
372 (Equation 7).

373  $BW = \log_2\left(\frac{SF_{0.5H}}{SF_{0.5L}}\right)$  ( $SF_{0.5H}$  &  $SF_{0.5L}$ : SFs at half-amplitude) (7)

374

375 Figure 7 illustrates the retinotopic organization of these bandwidth estimates. We observed a modest  
376 increase in the estimated bandwidth of tuning in parafoveal regions, compared to foveal regions,  
377 especially in V1. To quantify the relationship between eccentricity and tuning bandwidth, we  
378 collapsed the data across polar angle (Figure 8A). When dividing the data into equal sized eccentricity  
379 bins and examining the average tuning bandwidth as a function of eccentricity across subjects, a  
380 positive trend in V1-V3 was found (Figure 8B), with the correlation coefficients significantly greater

381 than zero in all three areas of V1 ( $t(7) = 8.31, p < 0.001$ ), V2 ( $t(7) = 5.84, p < 0.001$ ), and V3 ( $t(7) =$   
382  $5.14, p = 0.001$ ) (Figure 8C).

383  
384 To test for visual field anisotropies in SF tuning bandwidth, we conducted the same analysis  
385 previously described for the SF peak estimates. The changes of bandwidth with eccentricity for  
386 different quadrants are plotted in Figure 9. The statistical tests indicated significant differences  
387 between right and left quadrants in both V2 and V3 (V1:  $t(77) = -1.59, p = 0.12$ ; V2:  $t(73) = -2.14, p =$   
388  $0.04$ ; V3:  $t(64) = -2.86, p = 0.01$ ). However, there were no differences between either the horizontal  
389 and vertical quadrants (V1:  $t(74) = -1.21, p = 0.23$ ; V2:  $t(76) = 1.22, p = 0.23$ ; V3:  $t(68) = 0.29, p = 0.77$ ),  
390 or the upper and lower quadrants (V1:  $t(61) = 1.94, p = 0.06$ ; V2:  $t(63) = -0.06, p = 0.96$ ; V3:  $t(51) = -$   
391  $0.24, p = 0.81$ ).

392  
393 What relationship, if any, is there between pSFT peak preference and the corresponding bandwidth  
394 in human visual cortex? To examine this, we carried out a voxel-wise correlational analysis between  
395 these two parameters, and found a clear decline in bandwidth for voxels that prefer higher spatial  
396 frequencies (Figure 10A). Across all subjects, the negative correlation coefficients for pSFT  
397 bandwidth, in octaves, and pSFT peak proved significantly different from zero across all ROIs (V1:  
398  $t(7) = -10.05, p < 0.001$ ; V2:  $t(7) = -2.72, p = 0.03$ ; V3:  $t(7) = -4.43, p = 0.003$ ) (Figure 10B). To the best  
399 of our knowledge, this is the first report of an inverse relationship between spatial frequency  
400 preference and bandwidth within human visual cortex; an observation made possible by employing  
401 the model-based analysis approach.

402

403 Note that the derived relationships for estimated bandwidths in logarithmic scale (i.e. octave units)  
404 can change qualitatively when bandwidths are assessed in linear scale (i.e. cpd units). To explore the  
405 influence of the particular units used for assessing bandwidth, we assessed the bandwidth in cpd  
406 units, as well. The bandwidth in cpd units is equal to the full-width at half-maximum (FWHM) of the  
407 pSFT. Across subjects, the mean correlation between these cpd bandwidth values and eccentricity  
408 were, in V1-V3 respectively, -0.38 (SD=0.14), -0.2 (SD=0.10), and -0.31 (SD=0.16), suggesting a  
409 significant negative relationship (V1:  $t(7) = -7.55$ ,  $p < 0.001$ ; V2:  $t(7) = -5.65$ ,  $p < 0.001$ ; V3:  $t(7) = -5.4$ ,  
410  $p = 0.001$ ). In addition, the conversion of units led to a significant positive relationship between the  
411 FWHM and the pSFT peak (V1:  $t(7) = 18.95$ ,  $p < 0.001$ ; V2:  $t(7) = 26.02$ ,  $p < 0.001$ ; V3:  $t(7) = 22.63$ ,  $p <$   
412 0.001), with the mean correlations in V1-V3, respectively, being 0.65 (SD=0.10), 0.68 (SD=0.07), and  
413 0.68 (SD=0.09). Although the direction of these relationships appeared to be the reverse of what we  
414 had reported with the bandwidths in log scale (octaves), the estimated bandwidths in the two  
415 different scales were not inversely related. Mean correlation coefficients between bandwidth in  
416 octave units and FWHM in cpd units (V1: 0.16 (SD=0.15); V2: 0.29 (SD=0.22); V3: (0.24 (SD=0.18))  
417 were significantly positive in all three visual areas (V1:  $t(7) = 3.06$ ,  $p = 0.018$ ; V2:  $t(7) = 3.76$ ,  $p =$   
418 0.007, V3:  $t(7) = 3.73$ ,  $p = 0.007$ ). To shed light on this seemingly contradictory trend, we examined  
419 the interconnected relationship between mean values of the FWHM, bandwidth in log scale, and the  
420 pSFT peaks within different eccentricity (Figure 11). The direction of the relationship between  
421 FWHM and bandwidth in octave units depended on the pattern of modulation of the peak with  
422 eccentricity. The decline of the peak with eccentricity occurs along with an increase of the  
423 bandwidth in log scale, and a decrease of the FWHM.

424 **Discussion**

425 Estimation of voxel-wise spatial frequency tuning within human visual cortices has been proven  
426 difficult primarily due to methodological constraints –the variety and number of measurements  
427 necessary in order to fully capture a spatial frequency tuning function using traditional imaging  
428 approaches would be unreasonably time consuming. To circumvent this obstacle, we devised a  
429 computational approach paired with fMRI that allowed us to estimate the preference and shape of  
430 population spatial frequency tuning (pSFT), at a voxel-wise level. This generative model-driven  
431 analytic approach has the advantage that it allows for much more flexible and dynamic experimental  
432 designs, with event presentations and timing that would not be feasible when using conventional  
433 imaging designs (i.e. phase-encoding or stimulus-blocked designs). Here, we applied our novel  
434 approach to assess BOLD responses to the presentation of stimuli that rapidly changed in spatial  
435 frequency, in order to estimate pSFT functions across early visual cortex. Based on prior studies, we  
436 assumed that the pSFT took on the properties akin to a band-pass filter, with the pSFT for any  
437 particular voxel characterized by two key parameters: peak spatial frequency (cpd) and bandwidth  
438 (octave). With this approach, we were then able to thoroughly investigate the dependency of spatial  
439 frequency preferences on retinotopy, examining the precise relationship between voxel-wise spatial  
440 frequency preference and bandwidth, as well as its relation to the eccentricity of voxel-wise receptive  
441 field properties. Our results support previously reported declines in the peak SF with eccentricity in  
442 all visual areas (DeValois et al., 1982, Campbell et al., 1969, Movshon et al., 1978b). Interestingly, our  
443 findings suggest that the rate of peak spatial frequency decline is comparable across V1–V3. However,  
444 V1 appears distinct from extrastriate cortex in some domains, with the peak SF at the innermost  
445 eccentricity being higher in V1, which appears to drop across higher visual areas. The spatial  
446 frequency selectivity of the voxels appears to change with eccentricity as well, wherein estimated

447 bandwidths gradually become larger in more peripheral regions for all three areas of V1-V3.  
448 Moreover, comparison of the pSFTs between opposing quadrants of the visual field indicated a radial  
449 bias in the SF preferences of the voxels. We found higher sensitivities in horizontal and lower sides of  
450 the visual field in comparison to their opposite sides in V1. These patterns match with the previous  
451 reports of higher perceptual performances (Cameron et al., 2001; Carrasco et al., 2002; Rijksdijk et al.,  
452 1980; Levine and McAnany, 2005) and smaller pRF sizes in these sectors compared to the vertical and  
453 upper fields (Silva et al., 2018). Our results also pointed to higher peak SFs in the left field in V1 that  
454 is consistent with the previously reported smaller pRF sizes of this hemifield in V2 and V3 (Silva et  
455 al., 2018), and advantage of the left hemifield in detection task (Silva et al., 2008). We are aware,  
456 though, that the superiority of visual performance in the left visual field is not true for all types of  
457 stimuli and there has been reports of better performance of the right hemi-fields as well (Peyrin et  
458 al., 2005; Kitterle et al., 1992). This inconsistency, however, does not undermine the pattern that we  
459 have found, as our results are not completely devoid of such mismatch either; left visual field pSFTs  
460 have higher bandwidths in V2 which theoretically can result in poorer performance on this side.  
461 Future work directly comparing perceptual sensitivity across the visual field within an individual  
462 participant and comparing that to their pSFT estimates could shed further light on this. Finally,  
463 building upon previous results in the literature, we observed a novel relationship between the voxel-  
464 wise peak selectivity preference and tuning bandwidth, in which voxels that were responsive to  
465 higher frequencies had also tighter bandwidths. We should emphasize that the direction of the  
466 derived relationship between the bandwidth and the other parameters depended on the scale of the  
467 bandwidth; when we converted the scale of our measurements of the bandwidth from octave to the  
468 absolute units of cpd, the direction of the relationships switched.

469

470 The decline of the peak spatial frequency with eccentricity has been reported in neurophysiological  
471 studies of both cat and monkey (Movshon et al., 1978b, De Valois et al., 1982). In addition, the  
472 interdependency of the bandwidth and the peak that we observed is consistent with studies  
473 conducted within macaque visual cortices, wherein the bandwidth on octave scale appears to be  
474 inversely related to peak preference, but the bandwidth in linear scale is smaller for neurons that  
475 prefer lower SFs (De Valois et al., 1982, Foster et al., 1985). Interestingly, the negative correlation  
476 between bandwidth and eccentricity is not readily predicted from previous animal findings. Whereas  
477 De Valois et al. (1982) found no significant differences between bandwidths in foveal ( $<1.5^\circ$ ) and  
478 parafoveal ( $3^\circ$ – $5^\circ$ ) regions, Foster et al. (1985) reported a mean bandwidth of 1.8 octaves for the  
479 parafoveal region ( $2^\circ$ – $5^\circ$ ) and 1.4 octaves in foveal areas ( $<1^\circ$ ) of V1. Considering the gradual increase  
480 of bandwidth with eccentricity that we observed, these previously reported results do not contradict  
481 our findings. The mean bandwidths within the region-specific eccentricity bins that these previous  
482 studies examined ( $<5^\circ$ ) varies by 1–2 octaves in our study, and without having the measurements for  
483 all voxels we might have easily overlooked this relationship as well. However, by leveraging our pSFT  
484 technique across large swaths of visual cortex, our voxel-wise estimations can reveal an existing  
485 relationship that would otherwise be difficult to detect without obtaining detailed estimations of  
486 tuning profiles across a large population.

487

488 While human spatial frequency tuning has been estimated in previous studies (Henriksen et al. 2008;  
489 Singh et al., 2000; Sasaki et al., 2001), our approach differs in a number of meaningful ways, in terms  
490 of granularity or measurement, potential efficiency of time, and flexibility. First, none of the previous

491 neuroimaging work on SF tuning had been carried out to measure tuning for individual voxels.  
492 Henriksen et al. (2008) measured mean responses within bins comprised of voxels spanning one of  
493 three eccentricity ranges. With this approach, they concluded that SF preference is conversely  
494 dependent on eccentricity –a finding that squares with our results. Although these three points were  
495 sufficient for finding this relationship, our approach allows us to gather a richer dataset, bringing into  
496 focus a more fine-grained picture of tuning properties per voxel –additional details that further aid in  
497 understanding other aspects of frequency selectivity within human visual areas. For instance, our  
498 voxel-wise approach allowed us to examine the negative relationship between peak frequency and  
499 bandwidth of each voxel. In addition, we were able to detect an increase in bandwidth with  
500 eccentricity, which mostly occurred within the perifovea. Without the fine-grained sampling of  
501 eccentricity afforded by our paradigm, it would not have been feasible to detect such trends across  
502 retinotopic space.

503

504 In terms of efficiency, our method offers advantages, as well. Because traditional approaches involve  
505 discrete, repeated sampling of responses to a set of spatial frequencies, as was done in Henrikson et al.  
506 (2008), the upper bound of what could be measured within one scanning session was limited to the  
507 estimation of an average tuning curve per eccentricity range, for only three eccentricities. This is  
508 because traditional fMRI approaches, such as block designs and event-related designs, necessitate a  
509 fixed number of spatial frequencies, selected in advance, for which multiple measures are acquired. In  
510 theory, this traditional approach could yield a fine-grained picture of tuning properties, but in  
511 practice this would be much more time costly. In contrast, our model-driven paradigm allowed us to  
512 sweep through a broad range of spatial frequencies, allowing us to efficiently sample more

513 eccentricity ranges. In terms of flexibility, this model-based approach also allows us to, in principle,  
514 estimate tuning curves in the absence of any repeated instances of a particular spatial frequency  
515 presented. The flexibility of this approach thus lends itself nicely to experimental designs that were  
516 previously less feasible within the scanner, such as staircase procedures to estimate thresholds, or  
517 other dynamic experimental designs that have limited-to-no repeats of a given stimulus  
518 intensity/quality.

519

520 For first-order simplicity, our approach ignores a set of known nonlinearities, one nonlinearity in  
521 neurovascular coupling, and the other being inherent nonlinearities in neural response. Regarding  
522 neurovascular coupling, although we cannot deny that there are, in some regimes, nonlinear  
523 relationships between the BOLD signal and neural response, we do not believe the assumption of  
524 linearity is a determining factor in the qualitative patterns of results we report. Note that while the  
525 assumption of linearity between neural and BOLD response fails in certain regimes, the linearity  
526 approximation holds across quite a large range of conditions (Boynton et al., 1996). Indeed, this linear  
527 relationship is assumed in not only the lion's share of model-based approaches to fMRI analyses,  
528 including population receptive field mapping, but is the underlying assumption for the bulk of fMRI  
529 analyses. For simplicity, paucity of ground truth, and to adhere to the convention in fMRI analyses,  
530 we have opted to stick with the assumption of linearity, but acknowledge that the approach, along  
531 with most model-driven approaches, would benefit in the future from incorporation of a better  
532 model of the putative nonlinearity of neurovascular coupling (Buxton et al., 1998).

533

534 Regarding inherent neural nonlinearities, such as compressive nonlinearities brought about by  
535 temporal (Zhou et al., 2018) or spatial dynamics (Kay et al. 2013), we did not incorporate such  
536 nonlinearities into our current pSFT modeling procedure. Although it would certainly be interesting  
537 to incorporate spatiotemporal models to investigate how the preference of a particular voxel to a  
538 certain frequency is formed and how it is affected by the surrounding population, or extensions of  
539 time, these questions stand outside the scope of our current study, necessitating acquisition of  
540 compressive nonlinearities in the spatiotemporal domain, in order to properly test and constrain  
541 nonlinear models. Here, the focus was on estimating what frequency a particular voxel is most  
542 sensitive to, and its envelope of sensitivity. This does not imply that the nonlinear relationship  
543 between the peak and eccentricity is the product of such a nonlinearity that we have opted to overtly  
544 ignore. Rather, our estimated values represent the final sensitivity of a voxel, and we remain agnostic  
545 as to any spatiotemporal nonlinearities that may underlie this sensitivity. In other words, while the  
546 host of linear or nonlinear interactions that underlie each voxel's preference is not explained in our  
547 data set, and can be investigated in another set of studies and with a model incorporating such  
548 aspects, it is clear that the net preferences change with eccentricity.

549

550 Our approach rides on the assumption that all voxels within our target visual areas can be  
551 qualitatively characterized as band-pass filters. The weight of the evidence currently in the literature  
552 suggests that within most spatial frequency regimes, this band-pass filter assumption is reasonably  
553 accurate. Neuroimaging studies have shown that when the range of the spatial frequencies used in  
554 stimulating the occipital cortex is centered in the ideal low end of the spatial frequency spectrum for  
555 a particular visual area, then under these conditions most visual areas have been found to act as band-

556 pass filters (Henrikson et al., 2008, Singh et al., 2000). Furthermore, the majority of recorded cells in  
557 neurophysiological studies have been shown to be narrowly tuned, with only a low percentage being  
558 identified as truly resembling low-pass filters (Foster et al., 1985, De Valois et al., 1982). However,  
559 one potential follow-up to this study would be to model the voxel-wise pSFT using a combination of  
560 different filter types, to test the degree to which adding more complex, heterogeneous filter banks to  
561 the model could capture more variability in the BOLD response.

562

563 The typical spatial resolution of human fMRI experiments permits the measurement of population  
564 responses, with the pooled response of neurons within an individual voxel representing a wide range  
565 of spatial frequency preferences. Despite the much coarser scale of analyses accessible with fMRI, our  
566 pattern of results in humans succeed in demonstrating a high correspondence with the patterns often  
567 reported by animal studies using invasive recording techniques. Recently, similar computational  
568 modeling approaches have also been able to successfully estimate receptive field size in human visual  
569 cortex using solely fMRI measurements, while also demonstrating a close correspondence to direct  
570 measurements in nonhuman primates (Keliris et al., 2019). The high level of correspondence between  
571 these different methodologies and recording techniques offers strong support for the generative  
572 modeling approach employed in this study as a means for reproducing homologous animal  
573 electrophysiology results in human subjects.

574

575 **Figure Captions**

576

577 **Figure 1.** Stimulus and experimental procedure. A) Example stimuli varying in spatial frequency  
578 content. Each stimulus was generated by filtering uniform noise with a narrow band-pass filter that  
579 had a central spatial frequency equal to the desired spatial frequency content. The five presented  
580 frequencies are only a subset of 40 different frequencies that were used for data collection. B)  
581 Exemplar time course of stimulus presentation. During each run, subjects viewed a series of visual  
582 stimuli that changed constantly and rapidly. In spite of the temporal dynamics of the visual stimuli,  
583 the spatial frequency content of the stimuli remained the same for 1 TR, and then randomly changed  
584 to a new spatial frequency.

585

586 **Figure 2.** Schematic diagram of the proposed model-based approach. BOLD time series containing  
587 responses to varying spatial frequencies were both measured and synthesized. The synthesized BOLD  
588 response was calculated by convolving the hypothetical neural responses to the frequencies, i.e. the  
589 pSFT values at the tested frequencies with the HIRF. The pSFT was modeled as a log Gaussian  
590 function (Equation 1) with unknown mean ( $\mu$ ) and standard deviation ( $\sigma$ ). Through comparison of  
591 the measured BOLD response with the synthesized one, the unknown parameters of the pSFT were  
592 estimated. The  $R^2$  of the fit of the two time series is the index of similarity and the final estimated  
593 parameters are the outputs of a recursive optimization procedure, with the goal of maximizing the  
594 similarity index.

595

596 **Figure 3.** Voxel-wise map of the pSFT peak across the visual field. Each point represents a single  
597 voxel. The color codes the magnitude of the estimated pSFT peak of the voxel, and the size of the  
598 points are scaled with their  $R^2$  of the pSFT fits. The locations of the points are selected according to  
599 the pRF polar angle and eccentricity coordinates of the corresponding voxels. The symbols  
600 correspond to different subjects. In all three regions, the foveal voxels prefer the highest spatial  
601 frequencies and this value drops when moving toward the more peripheral regions. Moreover, the  
602 frequencies represented in V1 seem to be higher in comparison to the higher cortical regions.

603

604 **Figure 4.** Relationship between the pSFT peak and retinotopic eccentricity. (A) Peak of the pSFT  
605 declines with eccentricity in area V1. Each point is a voxel. Data from each subject is displayed with a  
606 certain color. (B) Mean subject-wise pSFT peak estimates within each eccentricity bin. Nine bins  
607 linearly spaced within the eccentricity range of [0.16°, 9.8°] have been used. Error bars show the  
608 standard error of the mean. (C&D) Parameters of the line that models the relationship between the  
609 peak pSFT and the eccentricity (both in logarithmic scale). Slopes and intercepts of such lines, fitted  
610 per subject on the binned data (bins similar to part B), are displayed in (C) and (D), respectively. The  
611 slopes are significantly less than zero in all three cortical regions. The intercept of the V1 area is  
612 significantly larger than this value in V3 area and almost significantly larger than the corresponding  
613 value in V2 (star symbol:  $p$ -value<0.05, double stars:  $p$ -value<0.001).

614

615 **Figure 5.** Comparison of model fits for peak-eccentricity relationship. The lowest  $\Delta AIC_c$  score across  
616 all visual areas of V1 to V3 belongs to the M-Inverse function. Performances of the Linear and H-  
617 Line models are very similar and poorer than the M-Inverse. Each bar shows the mean  $\Delta AIC_c$  value  
618 across all eight subjects and the error bars represent the standard error of the mean. Note that the  
619 values for the M-Inverse are very small (indicating the best candidate model) and not very variable,  
620 and thus difficult to see.

621

622 **Figure 6.** Comparison of peak SF between different quadrants of the visual field. Each column is a  
623 visual area (V1-V3), and row a comparison of retinotopic coverage. Specifically, each plot shows the  
624 mean estimated peak within an eccentricity bin, across subjects, for two opposing quadrant sets that  
625 are designated with red and blue colors in the insets of the plots on the left-hand column. In V1,  
626 horizontal, left, and lower quadrants have higher peaks in comparison with the vertical, right, and  
627 upper quadrants (horizontal vs. vertical:  $t(74) = 5.06, p < 0.001$ ; upper vs. lower:  $t(61) = -3.86, p <$   
628  $0.001$ ; right vs. left:  $t(77) = -3.67, p < 0.001$ ). Results of a t-test also revealed significant differences  
629 between upper and lower quadrants in V2 ( $t(63) = -2.32, p = 0.02$ ). Quadrant ranges include [-  
630  $45^\circ, 45^\circ]$ ,  $[45^\circ, 135^\circ]$ ,  $[135^\circ, 225^\circ]$ , and  $[225^\circ, 315^\circ]$ . Error bars represent +/- 1 standard error of the  
631 mean.

632

633 **Figure 7.** Voxel-wise map of the pSFT bandwidth estimates across visual field and area. Each point  
634 represents a single voxel. The color codes the magnitude of the estimated pSFT peak of the voxel, and  
635 the size of the points are scaled with their  $R^2$  of the pSFT fits. The locations of the points are selected  
636 according to the pRF polar angle and eccentricity coordinates of the corresponding voxels. The  
637 symbols distinguish data from different subjects. In all three areas the bandwidth is narrower in the  
638 foveal regions and increases slightly in the periphery.

639

640 **Figure 8.** Relationship between the pSFT bandwidth and retinotopic eccentricity. (A) Bandwidth  
641 increases slightly with eccentricity in V1. Each point illustrates a voxel. Data from every single  
642 subject has been displayed with a certain color. (B) Average of the mean pSFT bandwidth within each  
643 eccentricity bin, across subjects. Error bars show the standard error of the mean. (C) Distributions of  
644 the correlation coefficients between bandwidth and eccentricity, estimated per subject. Coefficients  
645 are significantly different than zero in all three areas (star symbol:  $p\text{-value}<0.05$ , double stars:  $p\text{-}$   
646  $\text{value}<0.001$ ).

647

648 **Figure 9.** Comparison of bandwidth estimates between different quadrants sets of the visual field. T-  
649 tests on the differences between right and left quadrants in V2 and V3 were significant (V2:  $t(73) = -$   
650  $2.14$ ,  $p = 0.04$ ; V3:  $t(64) = -2.86$ ,  $p = 0.01$ ). In other cases, the null hypothesis was not rejected.  
651 Quadrant ranges include  $[-45^\circ, 45^\circ]$ ,  $[45^\circ, 135^\circ]$ ,  $[135^\circ, 225^\circ]$ , and  $[225^\circ, 315^\circ]$ . Error bars represent  $+/-$   
652 1 standard error of the mean.

653

654 **Figure 10.** Voxels with higher pSFT peaks have narrower tuning. (A) Bandwidth decreases with  
655 increase in pSFT peak. Each point illustrates a voxel. Data from every single subject has been  
656 displayed with a certain color. (B) Distributions of the correlation coefficients between the peak and  
657 the bandwidth estimates of the pSFT, across subjects. The coefficients are significantly negative in all  
658 three regions of V1, V2, and V3 (double stars:  $p\text{-value}<0.001$ ).

659

660 **Figure 11.** Relationship between measures of bandwidths in octave scale, absolute full-width at half-  
661 max (FWHM), and peak spatial frequency preferences, over the eccentricity range. Tuning width, as  
662 measured by the absolute FWHM, decreases as a function of increasing eccentricity. However, when  
663 tuning width is expressed as octave bandwidths, we observed an increase of the bandwidth in  
664 logarithmic scale (BW) with eccentricity, as well as with the decrease of the pSFT peak, in V1-V3.  
665 Each point represents the average parameter estimates of voxels lying within an eccentricity bin, for  
666 an individual subject (symbols represent different subjects). The size of each point is inversely scaled  
667 relative to eccentricity, wherein largest points are near-eccentricities, and smallest are far  
668 eccentricities. Nine bins, equally distanced within the range of 0.16°–9.8°, were used in the analysis.

- 669    **References**
- 670
- 671    Birn, R. M., Saad, Z. S., & Bandettini, P. A. (2001). Spatial heterogeneity of the nonlinear dynamics in  
672        the FMRI BOLD response. *NeuroImage*, 14(4), 817–826.
- 673    Boynton, G. M., Engel, S. A., Glover, G. H., & Heeger, D. J. (1996). Linear Systems Analysis of  
674        Functional Magnetic Resonance Imaging in Human V1. *The Journal of Neuroscience*, 16(13),  
675        4207–4221.
- 676    Burnham, K. P., Anderson, D. R. (2002). Model selection and multimodel inference: a practical  
677        information-theoretic approach, 2nd edn. Springer, New York.
- 678    Buxton, R. B., Wong, E. C., & Frank, L. R. (1998). Dynamics of blood flow and oxygenation changes  
679        during brain activation: the balloon model. *Magnetic resonance in medicine*, 39(6), 855-864.
- 680    Cameron, E. L., Talgar, C. P., & Carrasco, M. (2001). Characterizing visual performance fields: effects  
681        of transient covert attention, spatial frequency, eccentricity, task and set size. *Spatial  
682        Vision*, 15(1), 61-75.
- 683    Campbell, F. W., Cooper, G. F., & Enroth-Cugell, C. (1969). The spatial selectivity of the visual cells  
684        of the cat. *The Journal of Physiology*, 203(1), 223–235.
- 685    Carrasco, M., Williams, P. E., & Yeshurun, Y. (2002). Covert attention increases spatial resolution  
686        with or without masks: Support for signal enhancement. *Journal of Vision*, 2(6), 467-479.
- 687    Cleland, B., Harding, T., & Tulunay-Keesey, U. (1979). Visual resolution and receptive field size:  
688        examination of two kinds of cat retinal ganglion cell. *Science*, 205(4410), 1015–1017.
- 689    Cohen, M. S. (1997). Parametric Analysis of fMRI Data Using Linear Systems Methods. *NeuroImage*,  
690        6(2), 93–103.

- 691 D'Souza, D. V., Auer, T., Frahm, J., Strasburger, H., & Lee, B. B. (2016). Dependence of chromatic  
692 responses in V1 on visual field eccentricity and spatial frequency: an fMRI study. *Journal of the*  
693 *Optical Society of America. A*, 33(3), A53–A64.
- 694 Brainard, D. H. (1997). The Psychophysics Toolbox. *Spatial Vision*, 10(4), 433–436.
- 695 De Valois, R. L., Albrecht, D. G., & Thorell, L. G. (1982). Spatial frequency selectivity of cells in  
696 macaque visual cortex. *Vision Research*, 22(5), 545–559.
- 697 Dumoulin, S. O., & Wandell, B. A. (2008). Population receptive field estimates in human visual  
698 cortex. *NeuroImage*, 39(2), 647–660.
- 699 Enroth-Cugell, C., & Freeman, A. W. (1987). The receptive-field spatial structure of cat retinal Y  
700 cells. *The Journal of Physiology*, 384(1), 49–79.
- 701 Everson, R. M., Prashanth, A. K., Gabbay, M., Knight, B. W., Sirovich, L., & Kaplan, E. (1998).  
702 Representation of spatial frequency and orientation in the visual cortex. *Proceedings of the*  
703 *National Academy of Sciences*, 95(14), 8334–8338.
- 704 Farivar, R., Clavagnier, S., Hansen, B. C., Thompson, B., & Hess, R. F. (2017). Non-uniform phase  
705 sensitivity in spatial frequency maps of the human visual cortex. *Journal of Physiology*, 595(4),  
706 1–25.
- 707 Foster, K. H., Gaska, J. P., Nagler, M., & Pollen, D. A. (1985). Spatial and temporal frequency  
708 selectivity of neurons in visual cortical areas V1 and V2 of the macaque monkey. *Journal of*  
709 *Physiology*, 365(1), 331–363.
- 710 Freeman, J., & Simoncelli, E. P. (2011). Metamers of the ventral stream. *Nature Neuroscience*, 14(9),  
711 1195–1204.

- 712 Friston, K. J., Jezzard, P., & Turner, R. (1994). Analysis of functional MRI time-series. *Human Brain*  
713 *Mapping*, 1(2), 153–171.
- 714 Glover, G. H. (1999). Deconvolution of impulse response in event-related BOLD  
715 fMRI1. *Neuroimage*, 9(4), 416-429.
- 716 Greve, D. N., & Fischl, B. (2009). Accurate and robust brain image alignment using boundary-based  
717 registration. *NeuroImage*, 48(1), 63–72.
- 718 Hansen, K. A., David, S. V., & Gallant, J. L. (2004). Parametric reverse correlation reveals spatial  
719 linearity of retinotopic human V1 BOLD response. *NeuroImage*, 23(1), 233–241.
- 720 Harvey, B. M., & Dumoulin, S. O. (2011). The Relationship between Cortical Magnification Factor  
721 and Population Receptive Field Size in Human Visual Cortex: Constancies in Cortical  
722 Architecture. *Journal of Neuroscience*, 31(38), 13604–13612.
- 723 Harvey, B. M., Klein, B. P., Petridou, N., & Dumoulin, S. O. (2013). Topographic representation of  
724 numerosity in the human parietal cortex. *Science*, 341(6150), 1123–1126.
- 725 Henriksson, L., Nurminen, L., Hyvarinen, A., & Vanni, S. (2008). Spatial frequency tuning in human  
726 retinotopic visual areas. *Journal of Vision*, 8(10), 5–5.
- 727 Hess, R. F., Li, X., Mansouri, B., Thompson, B., & Hansen, B. C. (2009). Selectivity as well as  
728 sensitivity loss characterizes the cortical spatial frequency deficit in amblyopia. *Human Brain*  
729 *Mapping*, 30(12), 4054–4069.
- 730 Hurvich, C. M., & Tsai, C.L. (1989). Regression and Time Series Model Selection in Small Samples.  
731 *Biometrika*, 76(2), 297–307.
- 732 Issa, N. P., Trepel, C., & Stryker, M. P. (2000). Spatial frequency maps in cat visual cortex. *Journal of*  
733 *Neuroscience*, 20(22), 8504–8514.

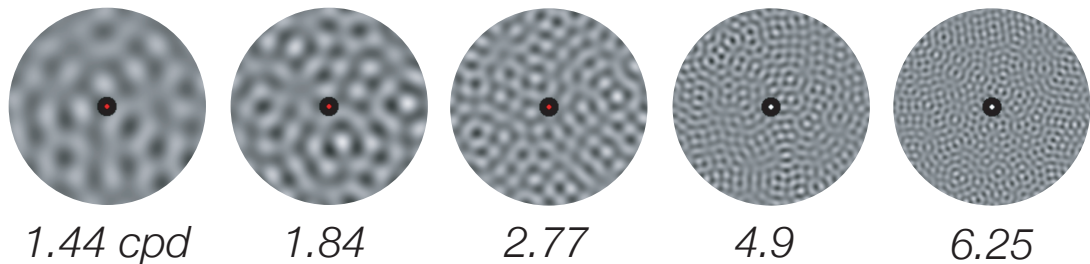
- 734 Kay, K. N., Naselaris, T., Prenger, R. J., & Gallant, J. L. (2008). Identifying natural images from human  
735 brain activity. *Nature*, 452(7185), 352–5.
- 736 Kay, K. N., Winawer, J., Mezer, A., & Wandell, B. A. (2013). Compressive spatial summation in  
737 human visual cortex. *Journal of Neurophysiology*, 110(2), 481-494.
- 738 Karim, A. R., & Kojima, H. (2010). The what and why of perceptual asymmetries in the visual  
739 domain. *Advances in Cognitive Psychology*, 6(6), 103-115.
- 740 Keliris, G. A., Li, Q., Papanikolaou, A., Logothetis, N. K., & Smirnakis, S. M. (2019). Estimating  
741 average single-neuron visual receptive field sizes by fMRI. *Proceedings of the National Academy  
742 of Sciences*, 116(13), 6425–6434.
- 743 Kitterle, F. L., Hellige, J. B., & Christman, S. (1992). Visual hemispheric asymmetries depend on  
744 which spatial frequencies are task relevant. *Brain and cognition*, 20(2), 308-314.
- 745 Kleiner, M., Brainard, D., & Pelli, D. (2007). What's new in Psychtoolbox-3? In *Perception 36 ECPV  
746 Abstract Supplement*.
- 747 Levine, M. W., McAnany, J. J., 2005. The relative capabilities of the upper and lower visual  
748 hemifields. *Vision Research*, 45(21), 2820–2830.
- 749 Moeller, S., Yacoub, E., Olman, C. A., Auerbach, E., Strupp, J., Harel, N., & Uğurbil, K. (2010).  
750 Multiband multislice GE-EPI at 7 tesla, with 16-fold acceleration using partial parallel imaging  
751 with application to high spatial and temporal whole-brain fMRI. *Magnetic Resonance in  
752 Medicine*, 63(5), 1144–1153.
- 753 Movshon, J. A., Thompson, I. D., & Tolhurst, D. J. (1978a). Receptive field organization of complex  
754 cells in the cat's striate cortex. *The Journal of Physiology*. 283(1), 79–99.

- 755 Movshon, J. A., Thompson, I. D., & Tolhurst, D. J. (1978b). Spatial and temporal contrast sensitivity
- 756 of neurones in areas 17 and 18 of the cat's visual cortex. *The Journal of physiology*, 283(1), 101-
- 757 120.
- 758 Nestares, O., & Heeger, D. J. (2000). Robust multiresolution alignment of MRI brain volumes.
- 759 *Magnetic Resonance in Medicine*, 43(5), 705–715.
- 760 Pelli, D. G. (1997). The VideoToolbox software for visual psychophysics: Transforming numbers into
- 761 movies. *Spatial Vision*, 10(4), 437–442.
- 762 Peyrin, C., Schwartz, S., Seghier, M., Michel, C., Landis, T., & Vuilleumier, P. (2005). Hemispheric
- 763 specialization of human inferior temporal cortex during coarse-to-fine and fine-to-coarse
- 764 analysis of natural visual scenes. *Neuroimage*, 28(2), 464-473.
- 765 Rijnsdijk, J. P., Kroon, J. N., & Van der Wildt, G. J., (1980). Contrast sensitivity as a function of
- 766 position on the retina. *Vision Research*, 20(3), 235–241.
- 767 Sasaki, Y., Hadjikhani, N., Fischl, B., Liu, A. K., Marret, S., Dale, A. M., & Tootell, R. B. H. (2001).
- 768 Local and global attention are mapped retinotopically in human occipital cortex. *Proceedings of*
- 769 *the National Academy of Sciences*, 98(4), 2077–2082.
- 770 Schira, M. M., Wade, A. R., & Tyler, C. W. (2007). Two-Dimensional Mapping of the Central and
- 771 Parafoveal Visual Field to Human Visual Cortex. *Journal of Neurophysiology*, 97(6), 4284–4295.
- 772 Schira, M. M., Tyler, C. W., Spehar, B., & Breakspear, M. (2010). Modeling magnification and
- 773 anisotropy in the primate foveal confluence. *PLoS Computational Biology*, 6(1), e1000651.
- 774 Schwartz, E. L. (1977). Spatial mapping in primate sensory projection: analytic structure and
- 775 relevance to perception. *Biological Cybernetics*, 25(4), 181–194.

- 776 Silva, M. F., Maia-Lopes, S., Mateus, C., Guerreiro, M., Sampaio, J., Faria, P., & Castelo-Branco, M.
- 777 (2008). Retinal and cortical patterns of spatial anisotropy in contrast sensitivity tasks. *Vision*
- 778 *Research*, 48(1), 127–135.
- 779 Silva, M. F., Brascamp, J. W., Ferreira, S., Castelo-Branco, M., Dumoulin, S. O., & Harvey, B. M.
- 780 (2018). Radial asymmetries in population receptive field size and cortical magnification factor in
- 781 early visual cortex. *NeuroImage*, 167, 41–52.
- 782 Singh, K. D., Smith, A. T., & Greenlee, M. W. (2000). Spatiotemporal Frequency and Direction
- 783 Sensitivities of Human Visual Areas Measured Using fMRI. *NeuroImage*, 12(5), 550–564.
- 784 Watanabe, A., Mori, T., Nagata, S., & Hiwatashi, K. (1968). Spatial sine-wave responses of the human
- 785 visual system. *Vision Research*, 8(9), 1245–1263.
- 786 Welbourne, L. E., Morland, A. B., & Wade, A. R. (2018). Population receptive field (pRF)
- 787 measurements of chromatic responses in human visual cortex using fMRI. *NeuroImage*, 167, 84–
- 788 94.
- 789 Wilson, H. R., Mcfarlane, D. K., & Phillips, G. C. (1983). Spatial frequency tuning of orientation
- 790 selective units estimated by oblique masking. *Vision Research*, 23(9), 873–882.
- 791 Xu, J., Moeller, S., Auerbach, E. J., Strupp, J., Smith, S. M., Feinberg, D. A., ... Uğurbil, K. (2013).
- 792 Evaluation of slice accelerations using multiband echo planar imaging at 3T. *NeuroImage*, 83,
- 793 991–1001.
- 794 Xu, X., Anderson, T. J., & Casagrande, V. A. (2007). How do functional maps in primary visual cortex
- 795 vary with eccentricity? *The Journal of Comparative Neurology*, 501(5), 741–755.

- 796 Yeo, B. T., Krienen, F. M., Sepulcre, J., Sabuncu, M. R., Lashkari, D., Hollinshead, M., ... Buckner, R.
- 797 L. (2011). The organization of the human cerebral cortex estimated by intrinsic functional
- 798 connectivity. *Journal of Neurophysiology*, 106(3), 1125–1165.
- 799 Yu, H. H., Verma, R., Yang, Y., Tibballs, H. A., Lui, L. L., Reser, D. H., & Rosa, M. G. P. (2010).
- 800 Spatial and temporal frequency tuning in striate cortex: Functional uniformity and
- 801 specializations related to receptive field eccentricity. *European Journal of Neuroscience*, 31(6),
- 802 1043–1062.
- 803 Zhou, J., Benson, N. C., Kay, K. N., & Winawer, J. (2018). Compressive temporal summation in
- 804 human visual cortex. *Journal of Neuroscience*, 38(3), 691-709.

*A.*



*B.*

